AIP | The Journal of Chemical Physics

Focus: Nucleation kinetics of shear bands in metallic glass

J. Q. Wang and J. H. Perepezko

Citation: The Journal of Chemical Physics **145**, 211803 (2016); doi: 10.1063/1.4966662
View online: http://dx.doi.org/10.1063/1.4966662
View Table of Contents: http://scitation.aip.org/content/aip/journal/jcp/145/21?ver=pdfcov
Published by the AIP Publishing

Focus: Nucleation kinetics of shear bands in metallic glass

J. Q. Wang[1] and J. H. Perepezko[2,a)]
[1]*Key Laboratory of Magnetic Materials and Devices, Ningbo Institute of Materials Technology and Engineering, Chinese Academy of Sciences, Ningbo 315201, China*
[2]*Department of Materials Science and Engineering, University of Wisconsin-Madison, 1509 University Avenue, Madison, Wisconsin 53706, USA*

(Received 13 June 2016; accepted 19 October 2016; published online 7 November 2016)

The development of shear bands is recognized as the primary mechanism in controlling the plastic deformability of metallic glasses. However, the kinetics of the nucleation of shear bands has received limited attention. The nucleation of shear bands in metallic glasses (MG) can be investigated using a nanoindentation method to monitor the development of the first pop-in event that is a signature of shear band nucleation. The analysis of a statistically significant number of first pop-in events demonstrates the stochastic behavior that is characteristic of nucleation and reveals a multimodal behavior associated with local spatial heterogeneities. The shear band nucleation rate of the two nucleation modes and the associated activation energy, activation volume, and site density were determined by loading rate experiments. The nucleation activation energy is very close to the value that is characteristic of the β relaxation in metallic glass. The identification of the rate controlling kinetics for shear band nucleation offers guidance for promoting plastic flow in metallic glass. *Published by AIP Publishing.* [http://dx.doi.org/10.1063/1.4966662]

I. INTRODUCTION

Since the discovery of metallic glasses (MGs) over half a century ago, their excellent mechanical properties, such as high strength, high hardness, and good elasticity, have attracted considerable interest.[1–6] However, most of the MGs are brittle and do not exhibit sufficient plasticity required for practical applications.[7–9] Understanding the plastic deformation mechanisms is of vital importance in improving the plasticity and designing new MGs with desirable mechanical properties. However, the deformation theories in crystals such as dislocations and twinning are invalid for amorphous materials because there are no translational or rotational periodic atomic structures. In addressing the deformation mechanisms in MGs, there have been numerous simulation studies and modeling analyses on the atomic arrangements in metallic glasses that have identified specific cluster motifs in an amorphous phase that can affect deformation.[10,11] The earliest comprehensive study by Argon was based upon detailed observations of the deformation of an amorphous bubble raft model binary system (i.e., two bubble sizes).[12,13] During dynamic deformation of the system, two distinct, independent shear transformation configurations (i.e., shear transformation zones, STZs) were identified as concentrated and diffuse with different activation barriers. More recent work on colloidal glass systems with one particle size also revealed the details of the deformation dynamics, but only one type of transformation site was observed to be active.[14] Besides the analog simulations, there have been a number of computational approaches to simulate glass structure and deformation response.[15,16] While these studies have offered insight into the details of the atom rearrangements under an imposed shear stress for specific interatomic potentials, the system sizes are small and the strain rates are exceedingly high so that the direct application of the findings to actual experimental conditions is somewhat unclear. Moreover, recent experimental studies have revealed the presence of nanoscale spatial heterogeneities in amorphous alloys that have not been considered in the simulations, but may affect deformation.[17–22]

Besides the simulation studies, many experiments show that the initiation, propagation, and interactions of shear bands (SBs) are responsible for the inhomogeneous plastic deformations.[1,3,4,7–9,13,23,24] A large plastic deformation level is always accompanied by a large number of shear bands[7–9] whereas for brittle failure only a few SBs are active. Therefore, the easy initiation of SBs appears to be one of the most important factors for the large plastic deformability. On the basis of shear transformation theory, the initiation of SBs is closely related to the STZs, the deformation units in metallic glasses.[25–27] In the current viewpoint, under an external stress, STZs will percolate, self-organize, and develop into SBs.[28] Thus, the kinetics of STZs is the key to the plastic deformation behavior of metallic glasses at temperatures lower than glass transition temperature, T_g.

The activation of STZs leading to the initiation of shear bands has been investigated in light of nucleation theory.[29–35] The formation of shear bands has also been evaluated based on a quasi-phase transition state model.[36] In the models, it is considered that the elastic energy of the machine-sample system is partially transformed to the increased energy in shear bands.[23] The undeformed metallic glass resides at lower energy states compared to the shear bands. As a result, external energy is required to initiate deformation by shear bands and overcome the elastic constraint of the surrounding

a)Author to whom correspondence should be addressed. Electronic mail: perepezk@engr.wisc.edu

undeformed matrix. In an other work based on an energy landscape perspective, Johnson *et al.* viewed the activation of STZs as akin to beta relaxation of metallic glasses involving transitions within a given energy basin and the percolation of STZs as akin to alpha relaxation that involves interbasin transitions.[19] Such an intriguing correlation was confirmed by Yu *et al.* where it was reported that the activation energy of STZs is almost the same as that of beta relaxation.[37] In an energy perspective, it is found that the elastic energy stored in metallic glasses upon compression before yielding is almost the same as the thermal energy absorbed by metallic glass before glass transition.[38,39] In a flow perspective, the role of temperature and stress is similar in changing the viscosity of a glass-forming liquid.[40] Thus, the activation of STZs is expected to follow a thermally activated behavior that is promoted by stress. However, the transition kinetics (e.g., nucleation rates, activation barrier, and site density) has received limited attention.[32]

In general, the volume of STZs is of the order of about 1-6 nm^3 and the thickness of shear bands is about 10 nm.[31,41–43] In the measurement of the kinetic processes at such a small length scale, instrumented indentation, particularly nanoindentation, is a powerful tool in studying the microscopic mechanical/dynamic behavior.[1,31,44] From the application of the instrumented nanoindentation technique, a multimodal shear band nucleation behavior was identified in the initiation of the first shear bands metallic glasses by systematically studying the first pop-in events during loading.[32] Only the first pop-in events are studied from widely spaced indents to ensure that they are isolated from each other. This is different from the avalanche characters of shear bands formed upon continuous loading where there are interactions between shear bands.[45] The nucleation kinetics behavior established in previous work was extended by applying different loading rates. The activation energy and characteristic volume of the STZs were determined for the multimodal nucleation behavior. The site density for each nucleation mode was also determined based on the nucleation theory formalism.

II. EXPERIMENTAL DETAILS

The $Zr_{60}Cu_{20}Fe_{10}Al_{10}$ (Zr BMG) and a $Fe_{57.6}Co_{14.4}B_{19.2}Si_{4.8}Nb_4$ (at. %) (Fe BMG) bulk metallic glass samples with a diameter of 5 mm were prepared from high purity (>99.9 wt. %) components in an arc-melting furnace. The ingots were turned over and remelted for 5 times to make sure the components were mixed homogeneously. The amorphous structure was characterized using X-ray diffraction with Cu K_α radiation and differential scanning calorimetry. Samples with a thickness of about 1 mm were cut from the as cast rod and then polished carefully using polishing powders down to 0.1 μm. For the Fe BMG the annealed condition was established by heating the sample to 540 °C which is just above T_g and cooling. The continuous loading nanoindentation experiments were carried out on a MTS Nano Indenter G200 machine equipped with a Berkovich indenter and the isoloading experiments (quickly ramp to a given load and hold) were carried out on a Shimadzu indentation machine equipped with a conical indenter with a radius of 2.5 μm. The maximum drift rate was set to be 0.05 nm/s before each measurement. Four loading rates, 0.05, 0.1, 0.67, and 2 mN/s, were applied to study the load-rate-dependent behavior. For each loading rate, more than 100 repeats were performed on the same sample to ensure that the results are statistically significant. A 30 μm spacing distance was applied for the loading points to avoid possible overlapping of strain fields between the neighboring indentations. The machine resolution of displacement is <0.01 nm and the load resolution is 50 nN. The indenter approaches the sample surface from a distance of 1 μm at a constant approach velocity 25 nm/s. The surface approach sensitivity is 50%. Once the sample surface contact is detected the indenter loads at a constant loading rate.

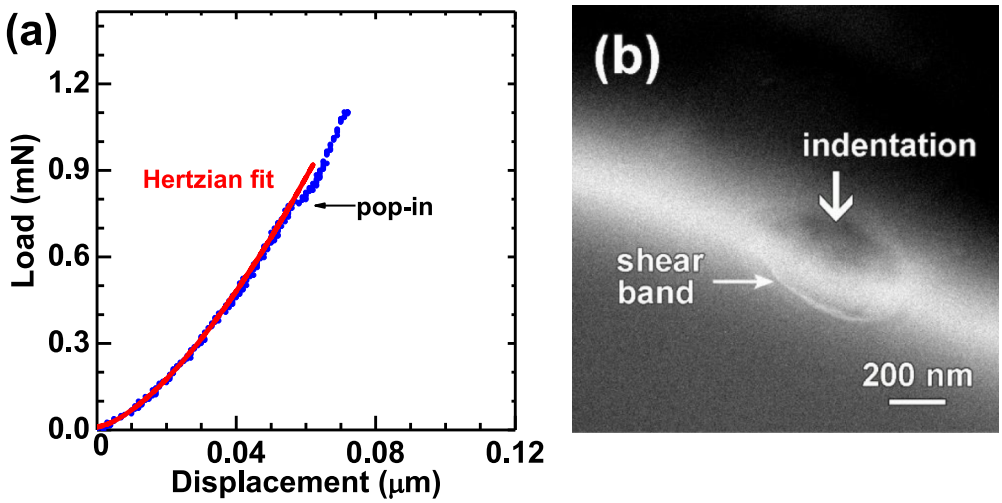

FIG. 1. Representative nanoindentation curve with a single pop-in and corresponding sample image with a single shear band for a $Zr_{60}Cu_{20}Fe_{10}Al_{10}$ BMG. (a) The nanoindentation trace with one pop-in, in the form of a load versus depth plot. The blue dots are the experimental data with a loading rate of 0.07 mN/s (spherical indenter with 2.5 μm radius), and the red curve is the fitting result according to Hertzian elastic contact theory. (b) The SEM image of the indentation. A single shear band can be seen clearly beneath the indentation. Reproduced with permission from Perepezko *et al.*, Proc. Natl. Acad. Sci. U. S. A. **111**, 3938 (2014). Copyright 2014 National Academy of Sciences.

III. RESULTS AND DISCUSSION

A. Detection of shear band nucleation

During nanoindentation, the material response is initially elastic following a Hertzian response in a load vs. displacement test.[2,44] The termination of the elastic response is marked by a pop-in event as shown in Fig. 1(a) where there is a rapid increase in displacement depth, h, at a constant load, P. In order to establish the relation between the first pop-in and shear band nucleation, a rectangular slab was machined in a $Zr_{60}Cu_{20}Fe_{10}Al_{10}$ (at. %) BMG and subjected to nanoindentation. As noted in Figs. 1(a) and 1(b), there is a correspondence between the first pop-in event and the initiation of a shear band.[32] Thus, the first pop-in event is associated with the threshold load (or stress) for shear band nucleation in the stressed volume under the indenter. To exclude the case of reactivation of pre-existing shear bands, the data collection was focused on only the development of the first shear band during loading.

Representative load-displacement indentation curves are shown in Figure 2 for a loading rate of 0.1 mN/s. The curves are shifted by 20 nm to distinguish each of them. Discrete jumps, namely pop-ins, in displacement can be observed during loading. Before the first pop-in event, the sample deforms elastically and the data can be fitted very well using the Hertzian elastic contact law[46,47]

$$P = \frac{4}{3} E_r R^{1/2} h^{3/2}, \tag{1}$$

where E_r is the reduced indentation modulus, h is the indentation depth, and R is the nominal contact radius of the indenter. The E_r is given by $E_r = \frac{E_s E_i}{E_i(1-\nu_s^2)+E_s(1-\nu_i^2)}$, where E_s (=107 GPa) and E_i (=1140 GPa) are the Young's modulus of the sample and the indenter, respectively; ν_s (=0.36) and ν_i (=0.07) are the Poisson's ratio of the sample and indenter, respectively. The modulus E_r is determined to be about 111 GPa, and the nominal contact curvature radius R is 744 ± 21 nm. The fitting results are shown as the solid magenta lines in Fig. 2. The first pop-in event can be clearly identified where the load-displacement profiles deviate from the fitted elastic curves.

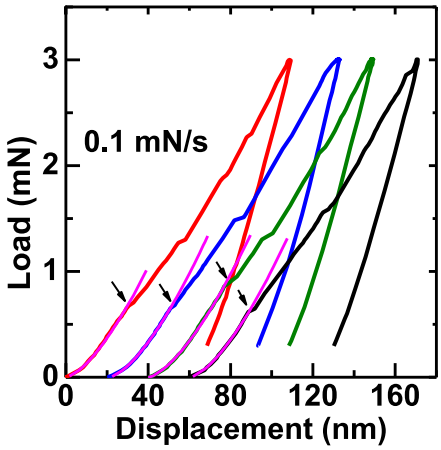

FIG. 2. Four representative nanoindentation curves in the form of load versus displacement. The magenta solid lines are the fitting results according to the Hertzian elastic contact law. The first pop-ins that deviate from the elastic contact behavior are marked by arrows.

B. Multimodal nucleation of shear bands

Since nucleation is a stochastic process, a proper study of shear band nucleation requires a statistically significant number of observations for analysis. During the mechanical testing of macroscopic bulk metallic glass (BMG) samples by conventional compression or tension methods, yielding below

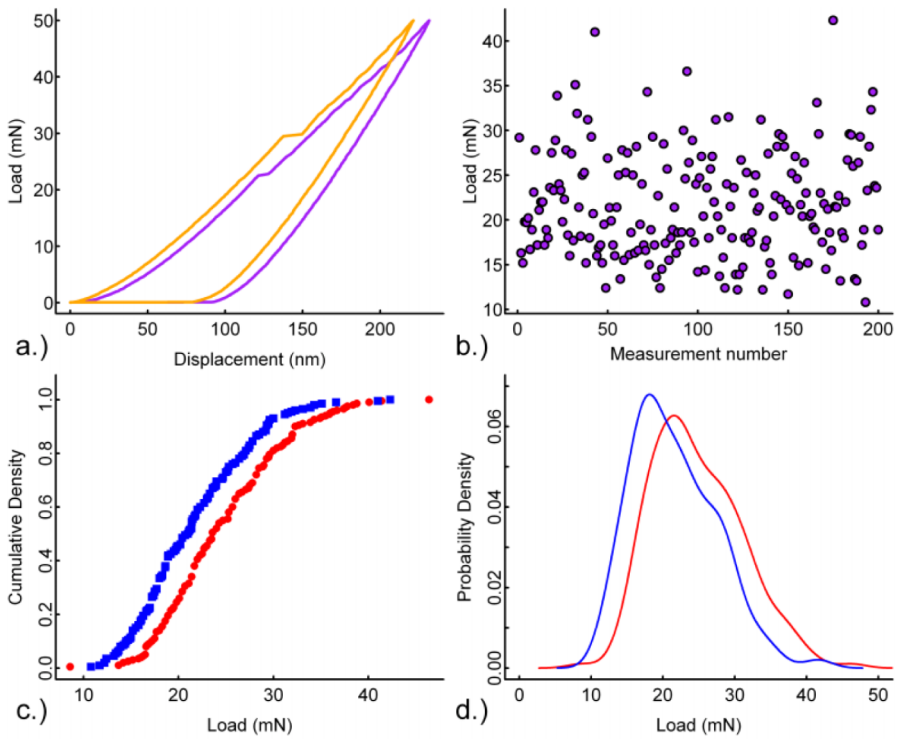

FIG. 3. The statistical analysis of the first pop-ins. (a) Two load-displacement traces from nanoindentation tests demonstrating the range of pop-in values under the same conditions (displacement of the solid curve has been offset by 10 nm for ease of viewing). (b) The observed data show no systematic drift over the course of experimentation. (c) Cumulative density and (d) probability density for as-cast (blue) and relaxed (red) Fe-BMG samples. Reproduced with permission from Perepezko *et al.*, Proc. Natl. Acad. Sci. U. S. A. **111**, 3938 (2014). Copyright 2014 National Academy of Sciences.

T_g occurs by shear band initiation and propagation that can be strongly influenced by loading conditions (such as sample alignment and machine stiffness) and material flaws (such as pores and inclusions) that mask the intrinsic sample behavior. Due to the small volume probed during a nanoindentation measurement, the method offers the important attribute to avoid the spurious influence of sample synthesis defects and uncertain loading conditions.

Based upon 100-200 individual nanoindentation measurements in each sample, a multimodal distribution character is demonstrated for the nucleation of shear bands[32] as shown in Figs. 3 and 4. Figure 3 presents the load versus pop-in data as a cumulative distribution and a probability distribution for a Fe BMG alloy in the as-cast and annealed condition where a distinct shoulder is present on the high load side of the distribution and the entire distribution shifts to higher loads after relaxation annealing. The same type of shift to higher loads after annealing was also reported by Wang *et al.*[48] The surface stress concentrations due to roughness are not the origin of shear bands since they are too localized to support shear band propagation that is necessary to trigger a pop-in event.[32] Moreover, if surface roughness were operating to promote shear bands the smooth translation of both peaks in the Fe-based BMG after annealing would not have been observed since the sample was re-polished after the annealing. Analysis of the data, in the order it was taken, shows no indication of a systematic drift over the course of the indentations (i.e., the data are uncorrelated) Fig. 3(b). While there is certainly a threshold load that must be crossed for shear band formation and propagation, the variability in the threshold load indicates that the process is in fact a stochastic one. In addition, in Figs. 4(a) and 4(b), two and three dimensional density plots are presented for the load at pop-in against the length of the pop-in. The probability density reveals the development of two maxima, which further supports the operation of a bimodal distribution of initiation sites. A similar bimodal distribution of first pop-in loads was reported by Zhao *et al.* for eight different BMG alloys, which suggests the bimodal character is a general behavior for shear band nucleation.[49]

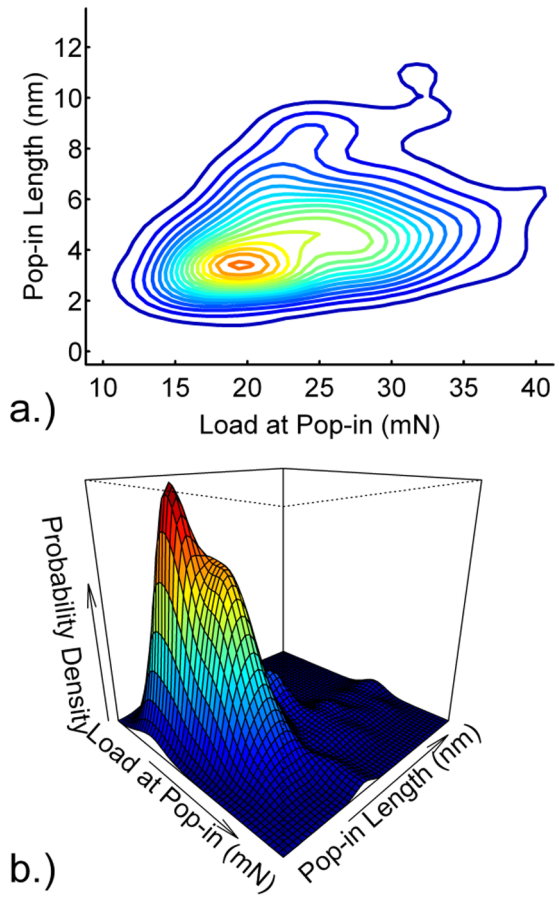

FIG. 4. Bimodal distribution of the first pop-ins for Fe BMG. Bivariate probability density plots shown as (a) 2D contours and (b) 3D wiremesh as a function of load at pop-in and pop-in length. There is a distinct peak as a shoulder on the high-load side of the data. In (a) the main peak can be observed at approximately 19 mN and 3 nm. A secondary peak can also be observed at approximately 27 mN and 4 nm. From these figures it is seen that the natural trend for the length of pop-in to increase with the load means that when projected onto the load axis, part of the bimodal nature that is more obvious in the two dimensional plot is obscured. Reproduced with permission from Perepezko *et al.*, Proc. Natl. Acad. Sci. U. S. A. **111**, 3938 (2014). Copyright 2014 National Academy of Sciences.

For the Zr BMG, a bimodal analysis containing two Gaussian distributions was also applied, as shown in Fig. 5(a). The corresponding frequency curves (Gaussian functions) versus load are shown in Figure 5(b). A clear shift to higher loads can be observed when the loading rate increases from 0.05 mN/s to 2 mN/s which is the same trend reported by Tönnies *et al.* for a Pd MG.[50] For each loading rate, the bimodal frequency curve was decomposed to show the two modes, one low-load mode (black data) and one high-load mode (red data), as shown in Figures 5(c)-5(f). The contribution of the low-load mode to the first pop-in events tends to increase, while the contribution from the high-load mode decreases with increasing loading rate.

To examine the strain rate effect on the two deformation modes, the equivalent strain rate, $\dot{\gamma}$ can be obtained from the loading rate, $\dot{P}$ by Ref. 31, $\dot{\gamma} = \frac{\dot{P}}{P}$. Then, the bimodal frequency distribution can be plotted versus strain rate, as shown in Fig. 6. The soft mode peak (located on the low-load side, black squares) is found to reside on the high strain rate side. With increasing strain/load rate, the contribution of the soft mode becomes larger. This indicates that in the soft mode discrete pop-in behavior is preferred at high strain rates. The hard mode peak (located on the high load side, red circles) can develop even at a low strain rate.

The results show that the nucleation of shear bands is represented by a bimodal mechanism. Given the close relationship between the atomic structure and the mechanical properties,[51,52] the bimodal nucleation behavior of SBs can be attributed to the local spatial heterogeneities in both the atomic structure and the dynamic characters in glassy materials.[17,18,20,37,50,53] The initiation of the shear bands may start from different sites, giving multiple modes of the first pop-in behavior. The loose packed structures that have more free volume will likely show a more viscoelastic behavior, while the dense packed structures deform more rigidly like an elastic spring.[53] The mechanical behavior of the loose packed structures exhibits a relatively strong strain rate dependence, while the rigid dense packing structures have a weak strain rate dependence.[13,24]

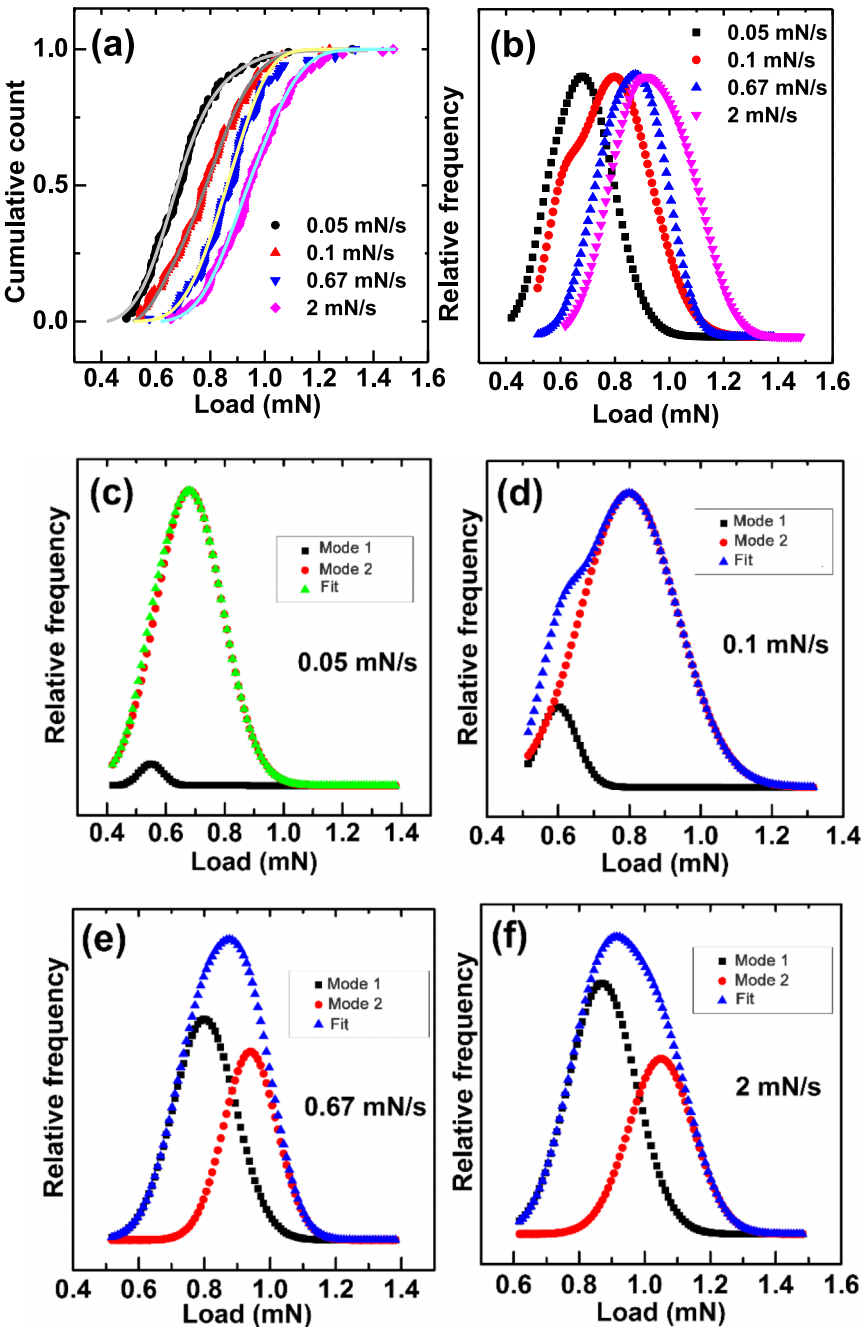

FIG. 5. (a) The cumulative distribution of experimental data and bimodal fitting of the first pop-ins versus the load for Zr BMG; (b) the frequency distribution of the bimodal fitting results; (c)-(f) the separate plots of the distribution frequency of the two modes at four loading rates.

C. Nucleation kinetics of shear bands

The use of load-time transformation diagrams to illustrate the nucleation behavior of shear bands is presented in Fig. 7 for continuous loading and isoloading conditions. Figure 7(a) shows the load-time diagram for the continuous loading experiments. With increasing loading rate, the shear banding onset stresses for both the high-load and low-load modes increase, which is similar to the behavior of crystallization reactions where the crystallization temperature increases with faster heating rate and is characteristic of thermally activated behavior. The evolution of shear bands upon iso-loading was studied using a spherical indenter with a radius of 2.5 μm. As shown in Figure 7(b), after loading up to the destination stress, the displacement is recorded versus time. As noted by Liu *et al.*, a delay time was observed before pop-in initiation.[54] The delay time for the first pop-in under a selected iso-load level is recorded and the distribution frequency is shown versus time, in Fig. 7(c). Bimodal distributions are found for the three studied loads. The iso-loading data of the first pop-ins in the diagram of load versus time are shown in Fig. 7(d). The load-time-transformation curve is very similar to the temperature-time-transformation for transformation from a low temperature phase to a high temperature phase where both the driving free energy and the diffusion rate increase with increasing temperature. It is worth noting that such an iso-loading nucleation of shear bands is also observed on compressing micropillars.[55,56] The nucleation of shear bands upon iso-loading is believed to derive from the stress assisted thermally activated plastic flow.[39]

Based on the cooperative shear model developed by Johnson and Samwer,[27] Pan *et al.*[31] have measured the volume,

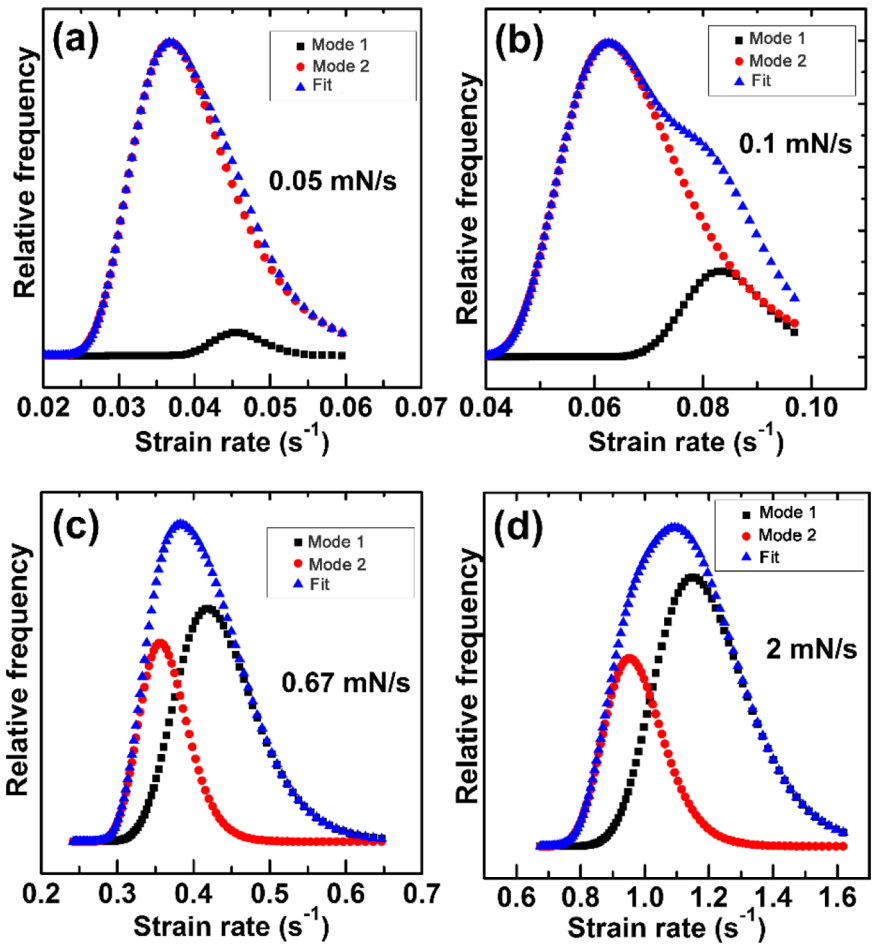

FIG. 6. The distribution frequency of the two modes versus nominal strain rate at four different loading rates for Zr BMG. The blue data represent the total distribution frequency of the two modes (black and red).

Ω of STZs using the strain-rate dependent hardness since there is a linear relation between hardness and yield strength.[57] Figure 8 shows the ln(τ) versus the ln(Equi. strain rate). The strain rate sensitivity of the pop-in stress

$$m = \frac{\partial \ln(\tau)}{\partial \ln(\dot{\gamma})} \tag{2}$$

can be determined to be 0.049 and 0.041, for the two modes, respectively. According to Ref. 27,

$$\Omega = \frac{kT}{G_0\gamma_C^2}\frac{1}{6R\zeta}\frac{1}{m\frac{\tau}{\tau_C}\left(1-\frac{\tau}{\tau_C}\right)^{1/2}}, \tag{3}$$

where k is the Boltzmann constant, T is the environment temperature, $G_0 = 30$ GPa is the shear modulus at 0 K, the average elastic limit $\gamma_C \approx 0.0267$, $R = 1/4$, $\zeta \approx 3$, $\tau/\tau_C = 0.912$ according to $\tau_{CT}/G = 0.0267 + \gamma_{C1}(T/T_g)^{2/3}$ with T = 300 K and $T_g = 675$ K.[27] The volume of STZ can be determined to be 3.15 nm^3 and 3.77 nm^3 for the low-load mode and high-load mode, respectively. According to Ref. 27 the activation energy, W, is given by

$$W = 4RG_0\gamma_C^2(1-\tau/\tau_C)^{3/2}\zeta\Omega. \tag{4}$$

The activation energies for the two modes are determined to be 1.29 eV and 1.54 eV for the low-load mode and high-load mode, respectively. The activation energy for the nucleation of shear bands is much higher than that for the nucleation of dislocations in the FCC crystalline metals (0.28–0.5 eV).[58] The activation volume is also much larger than that in the crystalline metals. This may be one reason why metallic glasses are usually more brittle than crystalline metals. It is interesting to note that the activation energy is close to the slow-β relaxation activation energies, ~24-26kT_g = 1.39-1.51 eV,[59] suggesting that the origins of STZs is possibly associated with the slow-β relaxation.

For the nucleation of shear bands, the site density of STZs is also an important parameter. It contributes to the attempt probability for the formation of shear bands and determines the final density of the SBs, and the transition of the deformation mechanism between inhomogeneous deformation and homogeneous flow. For the nucleation of shear bands from STZ sites that are randomly distributed with a site density of $m^* = \frac{the\ number\ of\ sites}{volume}$ in the deformed volume (V_{def}, the volume at a given load which satisfies the minimum criteria for a pop-in event) under the indenter tip, the site probability X is given by

$$X = 1 - \exp\left(-m^* V_{def}\right). \tag{5}$$

The deformed volume V_{def} is about 1% of V_{dis}, the volume displaced by the indentor.[60] The displaced volume is given by

$$V_{\mathrm{dis}} = \frac{\pi}{6}\left[3\left(\frac{9P^2R^5}{16E_r{}^2}\right)^{1/3} + \frac{9P^2}{16E_r{}^2R}\right]. \tag{6}$$

Then, the site density can be expressed as

$$m^* = -\frac{1}{V_{def}}\ln(1-X) = -\frac{1}{0.01V_{dis}}\ln(1-X). \tag{7}$$

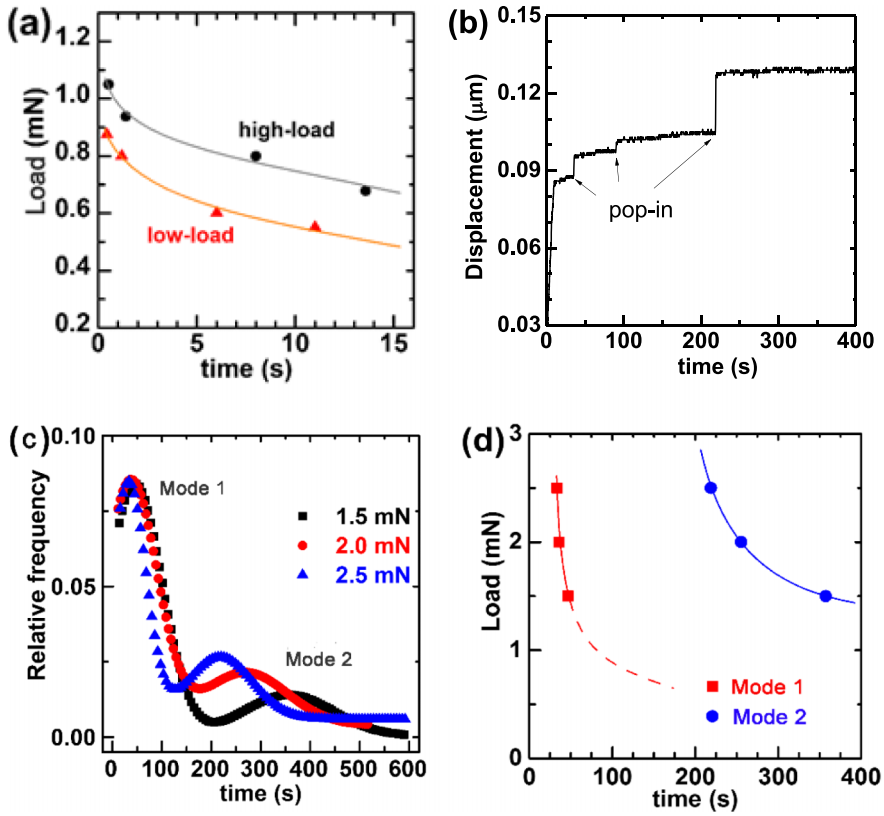

FIG. 7. (a) The continuous loading load-time transformation diagram for the nucleation of shear bands in Zr BMG. (b) The delay time for a shear banding event under isoloading. (c) The probability distribution of delay time for the first shear band. (d) The iso-load–time transformation diagram for the nucleation of shear bands.

The X value of the low-load mode, for example, is determined by its fraction of the total nucleation events at a given load, which is represented in Figs. 5(c)-5(f). The site density together with the relative frequency of the two nucleation modes is shown versus load in Fig. 9. The solid lines (black for low-load, red for high-load) represent the site density determined by Eq. (7). When the pop-in nucleation reaches a maximum, the site density is on the order of about 10^{19}–10^{20} m^{-3}. For shear band nucleation, the strain rate can be considered approximately as a driving frequency for transformation in thermally activated behavior, while the load/stress will change the height of the activation energy barrier. When the driven frequency is close to the intrinsic attempt frequency for a given biased energy barrier, the nucleation frequency will approach to a maximum.

For a relatively small difference of the nucleation barriers between the two modes, both of them seem to be activated with a different probability. The "hard" (high-load) mode can deform plastically in discrete behavior even at low loading rates, while the "soft" (low-load) mode can only deform plastically in discrete behavior at a high loading rate. The strain/load rate dependence of the two modes is akin to the heterogeneous to homogeneous deformation transformation in the Spaepen strain rate contours diagram.[24] The competition between the driving frequency and diffusive frequency can yield an inhomogeneous to homogeneous deformation transformation.[13] At a high strain rate an amorphous sample is more likely to deform inhomogeneously via shear bands rather than by homogeneous deformation.

In order to extract the nucleation rate from the observed first pop-in distributions, a kernel density for the probability density function, $f(t)$, is evaluated in terms of time, t, where the time is related to load at a constant loading rate. The smoothed $f(t)$ is then integrated in order to obtain the cumulative distribution function, $F(t)$. The hazard rate, $\lambda(t)$, represents the probability that a sample which had survived up until time t will have an event during the next Δt increment of time[61] and is defined as $\lambda(t) = f/(1-F)$. The hazard function is related to the nucleation rate, J, by $J = \lambda/V_e$, where V_e is the amount of volume at a given load which satisfies the minimum criteria for a pop-in event that is evaluated as $0.01V_d$, the volume deformed by the indenter.[32] Following the standard practice[1,12,13,24] J is related to an activation barrier by

$$J = \beta \exp\left(-\frac{\Delta W(\tau)^*}{kT}\right), \tag{8}$$

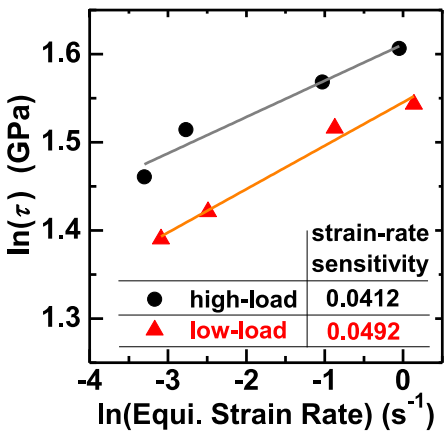

FIG. 8. The strain rate dependence of the stress at the first pop-ins for the two modes in the Zr BMG.

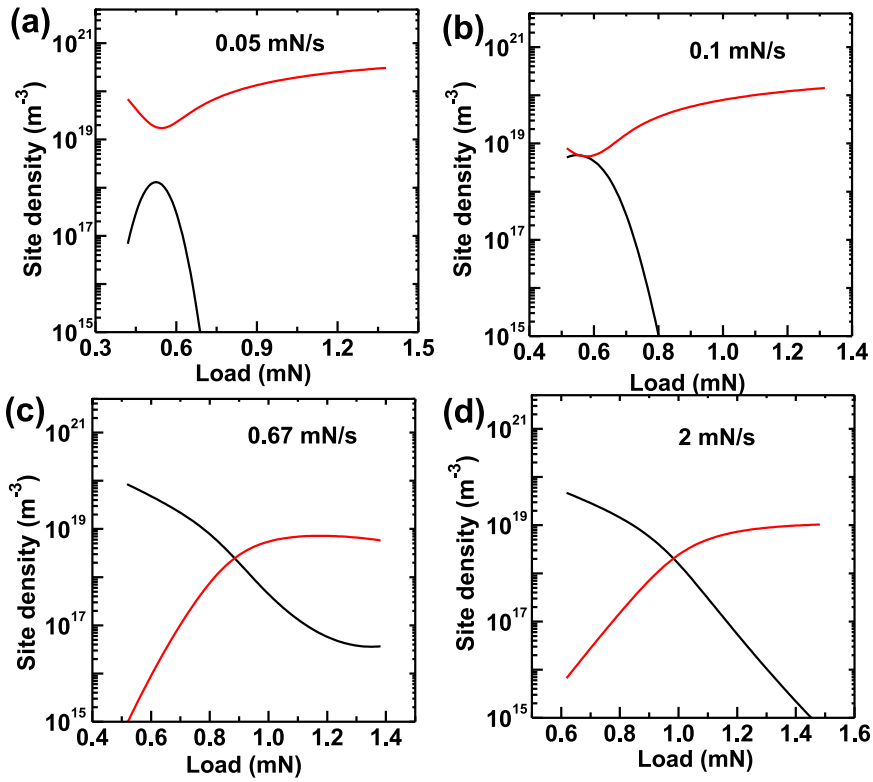

FIG. 9. The site density of the nucleation sites for the bimodal nucleation behavior of shear bands versus load for the Zr BMG.

where $\Delta W(\tau)^*$ is the activation barrier for shear band nucleation that is a function of the operating shear stress τ, and β is the frequency per unit volume which is the product of an attempt frequency taken as 10^{13} s^{-1} and the number density of sites. Based upon the character of the bimodal distribution of pop-in events, an independent evaluation can

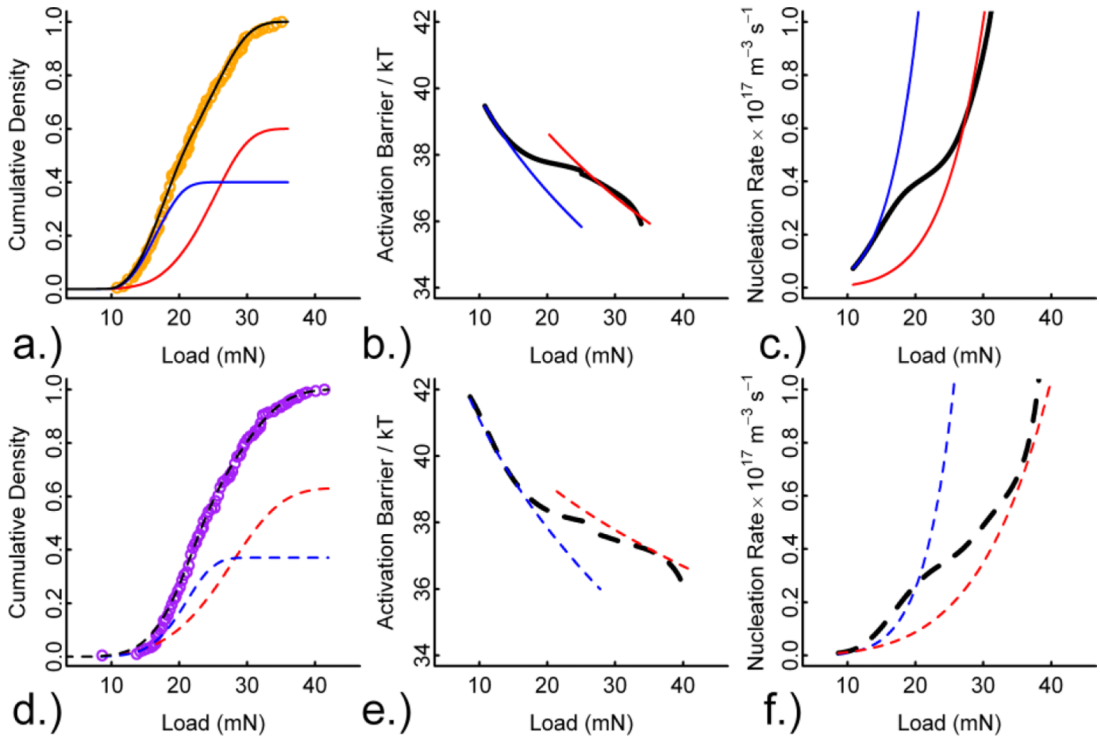

FIG. 10. The activation energy barrier and nucleation rates for the first pop-in events in the Fe-BMG sample. Parts (a)-(c) are for the as-cast sample and parts (d)-(f) are for the annealed sample. ((a) and (d)) The experimental cumulative density function is displayed together with the separately calculated contributions from each of the two nucleation sites. There is a close agreement between the fitted cumulative distribution and the measurements over the entire range including the endpoints. ((b) and (e)) The trend of activation barrier and the resultant nucleation rates as a function of load are separated and indicate the existence of two nucleation sites with an overlapping load range of operation. In the low load range where the nucleation barrier ranges from $42kT$ to $36kT$ the nucleation rate ((c) and (f)) reaches 0.4×10^{17} m^{-3} s^{-1} when a transition occurs to operation of the high load site. Reproduced with permission from Perepezko *et al.*, Proc. Natl. Acad. Sci. U. S. A. **111**, 3938 (2014). Copyright 2014 National Academy of Sciences.

be derived for the nucleation site density, m. For example, for the as-cast Fe BMG shown in Figure 3 and considering a Poisson distribution of nucleation sites within the volume, we obtain $m_L = 1 \times 10^{20}$ m^{-3} for the low load peak and $m_H = 9 \times 10^{19}$ m^{-3} for the high load peak. From the site density evaluation the activation barriers and nucleation rates can be determined as a function of load as shown in Fig. 10. From these results it is apparent that in order to identify shear band nucleation characteristics such as the bimodal distribution, it is necessary to obtain a significant dataset and analyze the full range of measurement. It is noteworthy that the site density of about 10^{20} m^{-3} derived from the nanoindentation experiments is consistent with the transition volume from shear band deformation to homogeneous flow in pillar compression tests reported by Volkert and Spaepen[62] and discussed by others.[63–65] As the volume decreases, the chance of having a shear band nucleation site decreases so that below the transition volume, the specimen is free of nucleation sites and homogeneous flow is the only available option for deformation.

In the analysis of shear band development, the models proposed by Argon[13] and Johnson and Samwer[27] relate the activation barrier for heterogeneous flow to the applied shear stress, τ. Often, in the analysis of the onset of plasticity and the deformation trajectory the path of maximum τ is considered to be controlling.[66] However, Packard and Schuh[60] have demonstrated that for amorphous alloys the appropriate path is the one in which τ is sufficient for both the initiation and propagation of shear bands. The operative τ along this path is related to the mean contact pressure, P_m, by $\tau \approx 0.07P_m$ which is determined from Hertzian mechanics. This allows for the scaling $\tau = CP^{1/3}$ with C a constant.

The Johnson and Samwer model considers the cooperative shear motion STZ's. Yielding occurs when the applied τ causes a critical density of minimum barrier STZ's to become unstable. The model expresses $W(\tau)^*/kT$ as in Equation (4) and with the scaling for τ yields

$$\frac{\Delta W(\tau)^*}{kT} = \frac{4RG_0\gamma_C^2\xi\Omega}{kT}\left(1 - \frac{\tau}{\tau_{C0}}\right)^{3/2} = M_{JS}\left[1 - A_{JS}P^{1/3}\right]^{3/2}. \quad (9)$$

This model has similarities to the concentrated shear mechanism of Argon.[13] In the Argon model, the concentrated shear mechanism is expected to operate at low temperature while at high temperature ($\geq 0.67T_g$) the diffuse shear mechanism should control homogeneous flow. For the diffuse shear transformation mechanism, the activation barrier is higher than that for the concentrated shear mechanism and is given by

$$\frac{W(\tau)^*}{kT} = \frac{\tau'\gamma_0^T\Omega}{kT}\left(1 - \frac{\tau}{\tau_{C0}}\right) = M_A\left[1 - A_AP^{1/3}\right], \quad (10)$$

where the parameters in Equations (9) and (10) are defined in Refs. 24 and 27, respectively. In order to compare the trends in Fig. 10 to the model predictions the stress independent terms, M_A, M_{JS}, A_A, and A_{JS} are treated as constant. The Johnson and Samwer model predicted trends of $\Delta W(\tau)^*/kT$ with load are indicated in Figs. 10(b) and 10(e) and provide a good agreement with the observed behavior in the low load range. The experimental data in the high load range do not extend over a wide enough range to determine clearly the stress dependence; however the trend is consistent with the Argon diffuse shear model. Moreover, the values of $\Delta W(\tau)^*$ that were determined at 300 K are comparable to the reported energy density results[47,67,68] and the activation energy ranges[47,59,69–71] for shear band activity reported in different amorphous alloys and reveal the important role of the applied stress in lowering

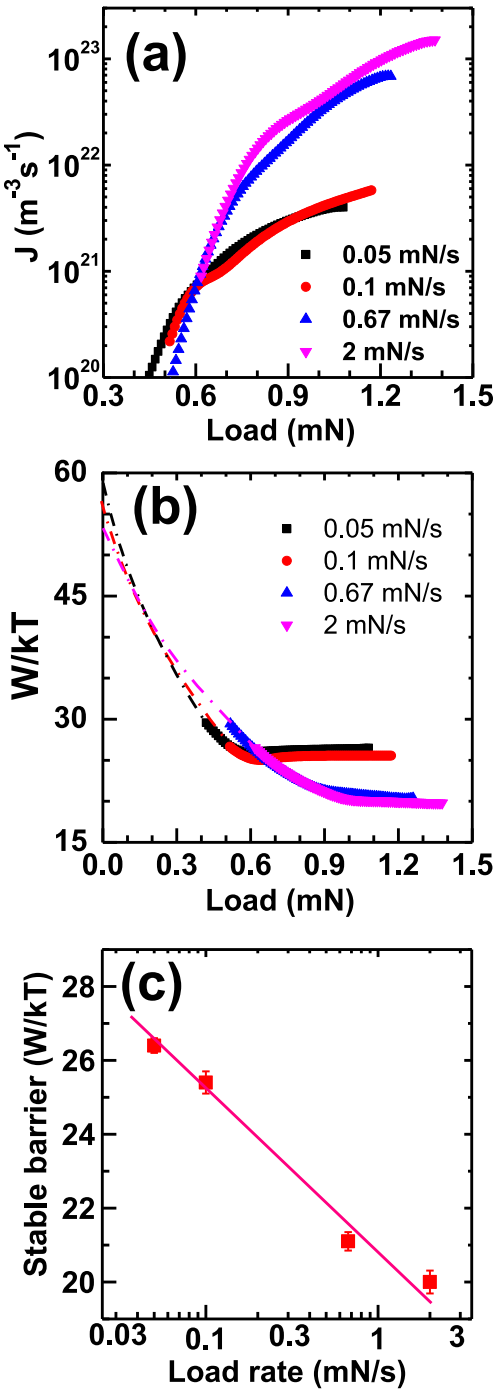

FIG. 11. (a) Nucleation rate vs. load for the Zr BMG. Increasing the loading rate increases the nucleation rate. (b) The normalized deformation barrier. The barrier decreases fast along with increasing load, until the activation barrier stabilizes. (c) The stabilized energy barrier versus the loading rate.

the barrier magnitude. Given that $J = \frac{\lambda}{V_{def}} = \frac{f/[1-F]}{0.01*V_{dis}}$, the nucleation rate of the Zr-based metallic glass at various loading rates is shown in Fig. 11(a). When the loading rate is high, the nucleation rate increases faster compared to that for slow loading rate. The activation barrier also stabilizes at the highest loads (Fig. 11(b)) and shows a correlation with the loading rate (Fig. 11(c)) that should allow for scaling.

While the representation of shear band nucleation in a standard form as in Equation (9) may be reasonable in a phenomenological sense, the kinetic events leading to the development of a viable shear band nucleus are not clear. For example, the observation of a delay time during the iso-load experiments indicates that there are atomic scale processes involved in the local structural organization leading to a shear band nucleus. The existing viewpoint indicates that an STZ in a favorable orientation with respect to the applied shear stress interacts through a strain field with neighbors to evolve into a nucleus in an autocatalytic manner. The kinetics of this process and the interpretation of the delay time require further development. Similarly, as more information on the structure of shear bands and the effect of variables such as composition on the deformation response becomes available[72–74] it should be possible to obtain a deeper understanding of the factors involved in the activation barrier and shear band nucleation.

IV. CONCLUSION

An approach to measure the nucleation kinetics of shear bands in metallic glasses has been established based upon instrumented nanoindentation and the observed first pop-in events. A multi-modal nucleation phenomenon was observed that contains at least two modes. The load/strain rate dependence denotes that the nucleation of shear bands exhibits thermally activated behavior. The derived activation energy is consistent with other reported results[75] and very close to that of the slow-β relaxation in metallic glasses. The nucleation sites are related to local spatial heterogeneities and both the site density and nucleation rates are found to be load and strain rate dependent. The identification of the rate controlling kinetics for shear band nucleation offers guidance for promoting plastic flow in metallic glass by enhancing the activity of nucleation sites that enable a homogeneous flow. The nanoindentation approach offers a promising potential to examine other metallic glass alloys and elucidate the influence of temperature, composition, state of relaxation, and other variables on shear band nucleation.

ACKNOWLEDGMENTS

The authors appreciate the discussions with Dr. S. Imhoff, the use of nanoindentation facilities in Professor M. W. Chen's laboratory, and the technical assistance from Dr. Y. H. Liu and Dr. M. R. Kolan. J.Q.W. would like to acknowledge the financial support from One-Hundred Talents Program of Chinese Academy of Science and NFSC-11504391. J.H.P. is grateful for the support of the ONR (Grant No. N00014-16-1-240).

[1]C. A. Schuh, T. C. Hufnagel, and U. Ramamurty, Acta Mater. **55**, 4067 (2007).
[2]M. W. Chen, Annu. Rev. Mater. Res. **38**, 445 (2008).
[3]W. H. Wang *et al.*, Intermetallics **67**, 81 (2015).
[4]A. Inoue and A. Takeuchi, Acta Mater. **59**, 2243 (2011).
[5]W. H. Wang, J. Appl. Phys. **110**, 053521 (2011).
[6]A. L. Greer, Y. Q. Cheng, and E. Ma, Mater. Sci. Eng. R **74**, 71 (2013).
[7]J. Das *et al.*, Phys. Rev. Lett. **94**, 205501 (2005).
[8]J. Schroers and W. L. Johnson, Phys. Rev. Lett. **93**, 255506 (2004).
[9]Y. H. Liu *et al.*, Science **315**, 1385 (2007).
[10]D. B. Miracle, Nat. Mater. **3**, 697 (2004).
[11]H. W. Sheng *et al.*, Nature **439**, 419 (2006).
[12]A. S. Argon and H. Y. Kuo, Mater. Sci. Eng. **39**, 101 (1979).
[13]A. S. Argon, Acta Metall. **27**, 47 (1979).
[14]P. Schall, D. A. Weitz, and F. Spaepen, Science **318**, 1895 (2007).
[15]M. Lee *et al.*, Acta Mater. **59**, 159 (2011).
[16]A. J. Cao, Y. Q. Cheng, and E. Ma, Acta Mater. **57**, 5146 (2009).
[17]Y. H. Liu *et al.*, Phys. Rev. Lett. **106**, 125504 (2011).
[18]H. Wagner *et al.*, Nat. Mater. **10**, 439 (2011).
[19]J. S. Harmon *et al.*, Phys. Rev. Lett. **99**, 135502 (2007).
[20]J. G. Wang *et al.*, Appl. Phys. Lett. **94**, 031904 (2009).
[21]L. Zhao *et al.*, Intermetallics **30**, 65 (2012).
[22]J. D. Plummer *et al.*, J. Non-Cryst. Solids **357**, 814 (2011).
[23]Z. Q. Liu *et al.*, Acta Mater. **59**, 7416 (2011).
[24]F. Spaepen, Acta Metall. **25**, 407 (1977).
[25]M. L. Falk and J. S. Langer, Phys. Rev. E **57**, 7192 (1998).
[26]J. S. Langer, Phys. Rev. E **70**, 041502 (2004).
[27]W. L. Johnson and K. Samwer, Phys. Rev. Lett. **95**, 195501 (2005).
[28]J. S. Langer, Scr. Mater. **54**, 375 (2006).
[29]C. A. Schuh and T. G. Nieh, Acta Mater. **51**, 87 (2003).
[30]C. A. Schuh and A. C. Lund, J. Mater. Res. **19**, 2152 (2004).
[31]D. Pan *et al.*, Proc. Natl. Acad. Sci. U. S. A. **105**, 14769 (2008).
[32]J. H. Perepezko *et al.*, Proc. Natl. Acad. Sci. U. S. A. **111**, 3938 (2014).
[33]S. Nachum and A. L. Greer, J. Alloys Compd. **615**, S98 (2014).
[34]I.-C. Choi *et al.*, Scr. Mater. **66**, 923 (2012).
[35]B. Yang, J. Wadsworth, and T. G. Nieh, Appl. Phys. Lett. **90**, 061911 (2007).
[36]S. T. Liu *et al.*, J. Non-Cryst. Solids **376**, 76 (2013).
[37]H. B. Yu *et al.*, Phys. Rev. Lett. **109**, 095508 (2012).
[38]Y. H. Liu *et al.*, Phys. Rev. Lett. **103**, 065504 (2009).
[39]B. Yang, C. T. Liu, and T. G. Nieh, Appl. Phys. Lett. **88**, 221911 (2006).
[40]P. F. Guan, M. W. Chen, and T. Egami, Phys. Rev. Lett. **104**, 205701 (2010).
[41]Y. Zhang and A. L. Greer, Appl. Phys. Lett. **89**, 071907 (2006).
[42]M. W. Chen *et al.*, Phys. Rev. Lett. **96**, 245502 (2006).
[43]S. T. Liu *et al.*, Scr. Mater. **67**, 9 (2012).
[44]W. C. Oliver and G. M. Pharr, J. Mater. Res. **7**, 1564 (1992).
[45]B. A. Sun and W. H. Wang, Prog. Mater. Sci. **74**, 211 (2015).
[46]K. L. Johnson, *Contact Mechanics* (Cambridge University Press, Cambridge Cambridgeshire, New York, 1985).
[47]K. Wang *et al.*, Mater. Trans. **47**, 1981 (2006).
[48]S. Wang *et al.*, J. Appl. Phys. **119**, 245113 (2016).
[49]X. N. Zhao *et al.*, J. Non-Cryst. Solids **445–446**, 19 (2016).
[50]D. Tönnies *et al.*, Appl. Phys. Lett. **106**, 171907 (2015).
[51]Y. Q. Cheng and E. Ma, Prog. Mater. Sci. **56**, 379 (2011).
[52]G. N. Greaves *et al.*, Nat. Mater. **10**, 823 (2011).
[53]J. C. Ye *et al.*, Nat. Mater. **9**, 619 (2010).
[54]Z. Y. Liu, Y. Yang, and C. T. Liu, Acta Mater. **61**, 5928 (2013).
[55]Z. Y. Liu *et al.*, Appl. Phys. Lett. **104**, 251901 (2014).
[56]Y. Yang *et al.*, Sci. Rep. **4**, 6699 (2014).
[57]C. A. Schuh and T. G. Nieh, J. Mater. Res. **19**, 46 (2004).
[58]C. A. Schuh, J. K. Mason, and A. C. Lund, Nat. Mater. **4**, 617 (2005).
[59]H. B. Yu *et al.*, Phys. Rev. B **81**, 220201 (2010).
[60]C. E. Packard and C. A. Schuh, Acta Mater. **55**, 5348 (2007).
[61]S. X. Song and T. G. Nieh, Intermetallics **19**, 1968 (2011).
[62]C. A. Volkert, A. Donohue, and F. Spaepen, J. Appl. Phys. **103**, 083539 (2008).
[63]H. J. Yu *et al.*, Adv. Funct. Mater. **23**, 4793 (2013).
[64]C. Q. Chen *et al.*, Phys. Rev. B **83**, 180201 (2011).
[65]J. R. Greer and J. T. M. De Hosson, Prog. Mater. Sci. **56**, 654 (2011).
[66]H. Bei, Z. P. Lu, and E. P. George, Phys. Rev. Lett. **93**, 125504 (2004).
[67]J. Q. Wang *et al.*, Phys. Rev. B **83**, 012201 (2011).
[68]Y. H. Liu *et al.*, Scr. Mater. **62**, 586 (2010).
[69]C. A. Schuh *et al.*, Philos. Mag. **83**, 2585 (2003).
[70]A. S. Argon and H. Y. Kuo, J. Non-Cryst. Solids **37**, 241 (1980).
[71]Y. F. Shi and M. L. Falk, Acta Mater. **55**, 4317 (2007).
[72]N. Nollmann *et al.*, Scr. Mater. **111**, 119 (2016).
[73]H. Rosner *et al.*, Ultramicroscopy **142**, 1 (2014).
[74]V. Schmidt *et al.*, Phys. Rev. Lett. **115**, 035501 (2015).
[75]L. Wang, Z. P. Lu, and T. G. Nieh, Scr. Mater. **65**, 759 (2011).